Mitigation of energy waste in pulsed jetting via valve-controlled auxiliary inlet

Xiaobo Bi[1] and Qiang Zhu [2,*]

[1]*Department of Mechanical Engineering, The Hong Kong Polytechnic University, Hung Hom, Kowloon, Hong Kong 999077, People's Republic of China*

[2]*Department of Structural Engineering, University of California San Diego, La Jolla, California 92093, USA*

Bioinspired jet propulsion through periodic jetting and refilling is a promising method to achieve high swimming speed with relatively low body stiffness. By using a fluid-structure interaction model, we demonstrate that it is possible to increase the efficiency of this locomotion mode by using a valve-controlled auxiliary inlet. The inlet is closed during the jetting phase yet opened during the refilling phase. Its primary function is to reduce the speed of the ingoing flow so that it takes much less energy to refill and the corresponding energy waste is mitigated. Our results show that a properly designed auxiliary inlet greatly reduces the cost of transport with very little sacrifice in swimming speed. For example, in a typical case the inclusion of such an inlet reduces the cost of transport by 60%, yet the decrease in forward speed is only 2.3%.

I. INTRODUCTION

Bioinspired soft-body robots, with their adaptability to complicated conditions and mitigated footprint in the environment, are promising tools for underwater exploration, environmental monitoring, and other aquatic operations [1,2]. A major setback for their application is the deficiency in their locomotion capacity in comparison with their counterparts with stiffer bodies using traditional propulsion techniques or fish-inspired swimming methods. Due to the relatively low body stiffness, these robots are usually not able to impart large forces on the surrounding fluid so that their ability for high-speed swimming and maneuvering is limited.

Recently it has been suggested that jet propulsion via body deformation may be the solution for enhanced swimming capacity of these robots [3–10]. This is attributed to the fact that in this particular swimming mode the hydrodynamic load is distributed over the whole body, rather than concentrated on a small portion of it (e.g., caudal or pectoral fins). Moreover, during jetting the hydrodynamic load is supported by the tension inside the body instead of its bending stiffness so that the demand on structural stiffness is much reduced.

In nature, jet propulsion is a locomotion mode employed by a variety of aquatic creatures such as jellyfish, cephalopods (squid, octopus, and cuttlefish), pelagic cnidarians, and tunicates such as sea salps. Among these creatures, the squid is one of the fastest swimmers in ocean. Small squids (e.g., the larvae of *Loligo vulgaris*) can achieve a bursting speed of 25 BL/s (body lengths per second) [11]. Larger squids (e.g., *Lologo opalescens*) can also reach a peak speed of 10 BL/s [12]. Species of flying squid can reach 40–50 BL/s in air [13,14]. In comparison, fish are limited to top speeds of approximately 25 BL/s [15]. On the other end of the spectrum, jellyfish display excellent swimming efficiency despite their relatively low swimming speed [16,17].

---

*qizhu@ucsd.edu
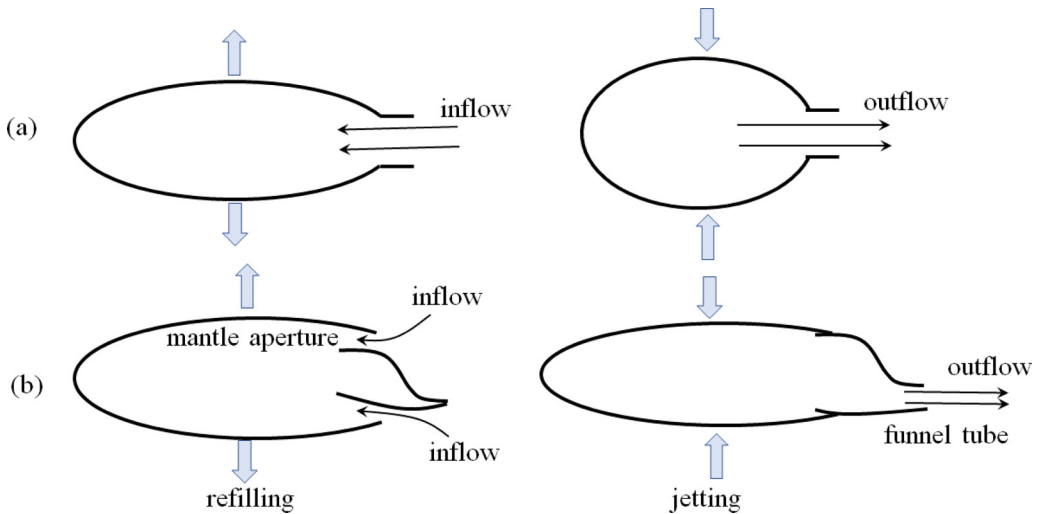
FIG. 1. Schematic of the refilling and jetting processes in (a) a squid-inspired robot [8] and (b) the actual squid.

Another notable feature is that some of these creatures, such as the squid, are able to point their jets in almost any direction so that changes in swimming direction can be achieved rapidly through thrust vectoring. This is expected to be a highly effective maneuvering method. Since it does not rely on control surfaces, which only work when there is sufficiently large forward speed, maneuvering forces can be generated with thrust vectoring even if there is little or no forward speed, as demonstrated with robotic devices [8,18,19] and numerical studies [20].

Due to the aforementioned advantages, biologically inspired aquatic robots capable of jet propulsion, especially those inspired by the squid, have recently attracted much attention [4–6,8,21,22]. However, most of the existing squid-inspired underwater systems swim around (or below) 1 BL/s, which is one order of magnitude slower than their natural counterparts. Besides, the energy efficiency of these systems is often low. A commonly accepted metric of energetic costs of animal locomotion is the nondimensional cost of transport, which is usually defined as the ratio between the power expenditure and the product of average speed and body weight. As an example, the cost of transport of a squidlike robot is 2.0 [22]. In comparison, the corresponding value of a squid with similar weight falls into the range of 0.4–0.6 [3], a jellyfish is in the range of 0.03–0.09 [3], and a fish is in the range of 0.09–0.7 [23].

An important cause of the poor performance of these robots as compared to their biological counterparts is the absence of the detailed flow control mechanisms used by living creatures. As illustrated in Fig. 1(a), a typical design of the existing prototypes features an empty chamber (the pressure chamber) in its body. A complete cycle in jet propulsion includes two phases, the inflation (refilling) phase and the deflation (jetting) phase. During the refilling phase the body expands to let water into the pressure chamber. During jetting the body shrinks to push water out of the pressure chamber to form a jet. With few exceptions [24], the existing designs use a single opening on the shell, which serves as both the inlet and the outlet so that the refilling flow and the jet flow are in opposite directions [see Fig. 1(a)]. A direct consequence is that in this scenario the kinetic energy of the refilling flow cannot be used in the deflation phase. As indicated in our recent numerical studies [25], the kinetic energy of the refilling flow, which comes from the work done by the body during inflation, is mostly dissipated due to viscosity and wasted.

It turns out that the low-efficiency problem associated with the reversal of the flow direction to refill and discharge the pressure chamber has already been solved in nature. An effective measure can be found in the swimming mechanism of squid. As sketched in Fig. 1(b), during inflation a squid

opens a wide inlet at the rim of its body called the mantle aperture for water intake. During deflation the mantle aperture is closed while a funnel tube is opened to serve as the nozzle. The cross-sectional area of the mantle aperture is much larger than that of the funnel tube so that the speed of the inflow is greatly reduced in comparison with that of the jet flow. This method effectively reduces the kinetic energy of the refilling flow (which is proportional to the square of the inflow speed), minimizing the energy losses during refilling.

There also exist other flow-control mechanisms to mitigate the energy waste for refilling. For example, in sea salps the flow inlet (the oral syphon) is placed at the front end of the body and the outlet (the atrial syphon) is at the rear end. The opening and closing actions of the inlet and outlet are controlled by valves. By synchronizing the actions of these valves with the body inflation and deflation, it is possible to create a predominantly unidirectional flow in the pressure chamber so that the energy spent in inflation actually enhances the jet flow via the internal flow it creates [26,27].

Yet another energy-saving method was proposed through variations in the size of the opening for water inflow and outflow [25]. During the refilling phase the body expands in the lateral direction and the opening is also enlarged. This effectively slows down the speed of the inflow and reduces its kinetic energy. On the other hand, during the jetting phase the opening shrinks to increase the jet speed for higher thrust, increasing the overall efficiency. This is reminiscent of the swimming method of jellyfish. However, a deformable opening is mechanically complicated and difficult to design considering the fact that in actual systems there could be rotatable nozzles for thrust vectoring.

In the present paper we investigate the possibility of efficiency enhancement of a squid-inspired swimmer by using an auxiliary flow inlet whose function is similar to that of the mantle aperture in real squid as shown in Fig. 1(b). This inlet is controlled by a valve that opens during refilling and closes during jetting. For mechanical simplicity the actions of this valve will be passive, i.e., its motion is driven entirely by the hydrodynamic load on it. Through numerical simulations, we will examine the feasibility of this performance-enhancement method, its potential benefit, and the requirement on the design of the valve.

The rest of the paper is organized as following. In the next section we describe the configuration and kinematics of the physical problem to be studied. The governing equations of the underlying fluid-structure interaction problem are then formulated. Since the method used in this paper has been well documented and validated in our previous publications [28,29], we will only include a brief description in this paper. In the results part, we present the performance of the system with the auxiliary inlet. A parametric study is also conducted to examine the effect of the design parameters of the valve. Finally, conclusions are drawn.

II. PROBLEM DESCRIPTION

The physical system we study is an idealized version of the robotic system developed by Christianson *et al.* [8]. The auxiliary inlet is inspired by the mantle aperture of a real squid [see Fig. 1(b)] as well as a similar design in a robotic system [24].

As shown in Fig. 2, we consider a freely swimming system with an axisymmetric geometry. It features an empty chamber enclosed within a deformable shell, an auxiliary inlet, and a cylindrical nozzle with diameter D and length L_1 (the exact geometry of the nozzle may affect the dynamics of the system [30], although this is not the focus of the current paper so that a simple nozzle shape is chosen). The contour length of the shell is fixed as L and the diameter of its orifice is fixed as D_0. This contour length is measured from rim to rim via the front of the shell so that the length of the curve representing the shell in the figure is $L/2$. Geometrically, we assume that this curve is part of an ellipse with a truncated end. The detailed mathematical derivation of the determination of this curve is included in our previous publication [29]. The thicknesses of the shell and the wall of the nozzle are assumed to be negligibly small.

The deformation of the shell is prescribed, yet the forward motion of the body itself is determined by Newton's law. To elaborate, in our system the expansion and contraction of the shell are achieved
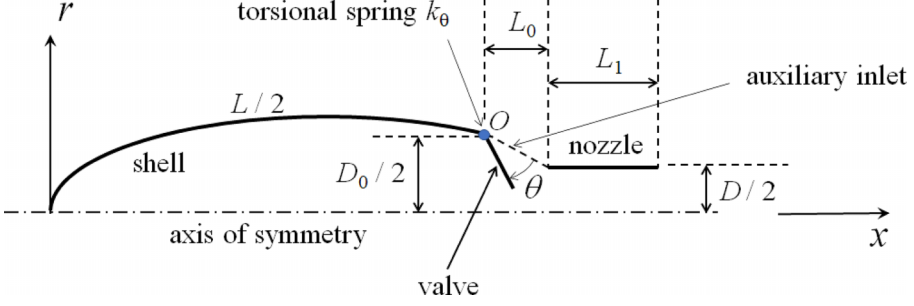
FIG. 2. Illustration of the squidlike swimmer with an auxiliary inlet controlled by a one-way valve.

by periodically varying the eccentricity of its contour curve so that during one deformation cycle $0 \leqslant t \leqslant T$ we have

$$e = e_0 + (e_1 - e_0)[1 - \cos(2\pi t/T)]/2, \tag{1}$$

where e_0 and e_1 are the eccentricities of the shell in the fully deflated and fully inflated states, respectively.

The opening and closing actions of the auxiliary inlet are controlled by a valve. For simplicity, this valve is modeled as a zero-thickness rigid plate capable of rotating around an axis O. At the axis there is a torsional spring with stiffness k_θ. The rotational inertia of the valve with respect to O is I_θ. The rotational angle θ is larger than or equal to zero so that the valve is only allowed to rotate inwards. When θ is zero the auxiliary inlet is completely closed and the spring is in its relaxed state. In addition, we set an upper limit of θ as $\pi/2 + \tan^{-1}[2L_0/(D_0 - D)]$, therefore the valve is not allowed to rotate past the horizontal position. This prevents the collision between the valve and the inner surface of the shell that could lead to numerical issues. It also helps avoid the scenario in which the valve is not able to rotate back during deflation when the spring k_θ is too weak.

III. MATHEMATICAL FORMULATIONS AND NUMERICAL APPROACH

To describe the hydrodynamics of the problem, we employ the axisymmetric Navier-Stokes equations with constant fluid density ρ and viscosity μ. The equations are defined within a cylindrical coordinate system $\mathbf{x} \equiv (x, r)$. As shown in Fig. 2, x is the longitudinal axis pointing from the head of the body towards the nozzle and r is the radial axis. We have

$$\rho\left(\frac{\partial u_x}{\partial t} + \mathbf{u} \cdot \nabla u_x\right) + \frac{\partial p}{\partial x} - \mu\left[\frac{\partial^2 u_x}{\partial x^2} + \frac{1}{r}\frac{\partial}{\partial r}\left(r\frac{\partial u_x}{\partial r}\right)\right] - f_x = 0,$$

$$\rho\left(\frac{\partial u_r}{\partial t} + \mathbf{u} \cdot \nabla u_r\right) + \frac{\partial p}{\partial r} - \mu\left[\frac{\partial^2 u_r}{\partial x^2} + \frac{1}{r}\frac{\partial}{\partial r}\left(r\frac{\partial u_r}{\partial r}\right) - \frac{u_r}{r^2}\right] - f_r = 0$$

$$\frac{\partial u_x}{\partial x} + \frac{1}{r}\frac{\partial(ru_r)}{\partial r} = 0, \tag{2}$$

where $\mathbf{u} \equiv (u_x, u_r)$ is the flow velocity vector, p is the pressure, and $\mathbf{f}(\mathbf{x}, t) \equiv (f_x, f_r)$ stands for the fluid-structure interaction force density, which is introduced to enforce the no-slip and no-flux boundary conditions at the fluid-structure interface in the immersed boundary framework [31–34]. Following the conventional treatment, $\mathbf{f}$ is obtained by distributing the hydrodynamic loading on the structure $\mathbf{F}$ (defined in the Lagrangian coordinate s) through a Dirac delta function so that

$$\mathbf{f}(\mathbf{x}, t) = \int_\Gamma \mathbf{F}(s, t)\delta(\mathbf{X}(s, t) - \mathbf{x})ds, \tag{3}$$

where Γ represents the entire Lagrangian domain including the shell (Γ_s), the nozzle (Γ_n), and the valve (Γ_v). $\mathbf{F}$ is assessed by using two sets of Lagrangian points [35,36]: the actual Lagrangian point attached to the structure [$\mathbf{X}(s)$] and the virtual Lagrangian point that moves with the local flow [$\tilde{\mathbf{X}}(s)$],

$$\mathbf{F}(s,t) = \alpha[\tilde{\mathbf{X}}(s,t) - \mathbf{X}(s,t)] + \beta[\tilde{\mathbf{U}}(s,t) - \mathbf{U}(s,t)], \tag{4}$$

in which $\mathbf{U}$ and $\tilde{\mathbf{U}}$ are, respectively, the structural velocities of the two Lagrangian points, i.e.,

$$\mathbf{U}(s,t) = \frac{\partial \mathbf{X}(s,t)}{\partial t}, \quad \tilde{\mathbf{U}}(s,t) = \int_{\Omega_f} \mathbf{u}(\mathbf{x},t)\delta[\mathbf{x} - \tilde{\mathbf{X}}(s,t)]d\mathbf{x}. \tag{5}$$

Ω_f is the fluid domain. α and β are negative constants with sufficiently large absolute values so that the difference between $\mathbf{X}(s)$ and $\tilde{\mathbf{X}}(s)$ can be minimized when $\mathbf{F}(s)$ converges after iterations. If properly chosen, the specific values of the two constants have negligible effect on the results.

The swimming of the system is a semiactive process. On the one hand, the deformation of the shell is prescribed in Eq. (1). On the other hand, the forward motion of the whole system and the rotation of the valve are passively driven by the hydrodynamic load. The dynamics of these passive motions are depicted by the balance of momenta in the horizontal direction and the angular direction, respectively. We have

$$m_b \frac{d^2 x_b}{dt^2} = F_b, \quad I_\theta \frac{d^2\theta}{dt^2} + k_\theta \theta = M_\theta, \tag{6}$$

where m_b is the total mass of the system and x_b is the displacement of the center of mass of the system in the $-x$ direction. I_θ denotes the moment of inertia of the valve with respect to the axis O, and k_θ represents the stiffness of the torsional spring. F_b is net horizontal hydrodynamic force on the body obtained as

$$F_b = -\int_\Gamma 2\pi r(s) F_x(s,t) ds, \tag{7}$$

where F_x is the x component of $\mathbf{F}$. M_θ is the moment acting on the valve by the ambient fluid calculated by

$$M_\theta = -\int_{\Gamma_v} 2\pi r(s)\mathbf{F}(s) \cdot \mathbf{r}(s) ds, \tag{8}$$

where $\mathbf{r}$ is the arm of the force $\mathbf{F}$ with respect to the spin axis O. For simplicity, when calculating the center of mass we assume that the mass is evenly distributed on the shell while the masses of the valve and the nozzle are not considered. The effect of the unsteady motions of point O on the rotation of the valve is not considered either since we assume that the acceleration of O is relatively small in comparison with the unsteadiness of the flow field near the valve so that the hydrodynamic load is the dominant driving effect of valve rotation (this is true when the acceleration of the body is small compared with the local acceleration of the fluid near the valve). Our numerical tests have confirmed that this effect is much smaller than the hydrodynamic one.

The locomotion performance is characterized by two parameters, the mean forward speed $\bar{u}_b$ and the cost of transport C_{trans}. $\bar{u}_b$ is defined as the time-averaged value of the forward speed $u_b \equiv \dot{x}_b$. C_{trans} is defined as E/l, where E is the energy expenditure obtained by integrating the power P required to activate the shell ($P = \int_{\Gamma_s} 2\pi r\mathbf{F} \cdot \mathbf{U} ds$) over a certain duration of time and l is the traveled distance during the same time slot. In practice, both $\bar{u}_b$ and C_{trans} are calculated within one deformation cycle after the steady state has been established.

The conventional definition of C_{trans} also includes the body mass (or the body weight) [17]. However, once the steady state is established, the body mass plays a very small role in determining either the forward speed (which is determined by the balance between thrust and drag) or the power expenditure when the body deformation is prescribed. Subsequently, in our case the mass of the

TABLE I. Physical parameters in the model.

e_0	e_1	D_0	D	L_0	L_1	m_b	μ
0.9	0.7	0.15	0.10	0.05	0.10	0.001	0.001

swimmer m_b has little effect on E or l. If we use the conventional definition of C_{trans}, its value can be easily manipulated by varying m_b so that the results might be misleading.

To numerically solve the problem, we discretize the hydrodynamic equations by using a second-order algorithm in the spatial domain and a Crank-Nicholson algorithm in the time domain. The discrete equations are then solved with a traditional projection method, in which the flow velocity and pressure are decoupled by using the block lower triangular–upper triangular decomposition method. The general process to update the flow field can be summarized as follows: (1) an intermediate flow field is first obtained with the known flow velocity and pressure from the previous time step; (2) the pressure field is updated by using the predicted flow field through the elliptic pressure equation; (3) the velocity field is then updated by using the intermediate velocity and the updated pressure. An iteration algorithm is applied to achieve the coupling between the passive motions and hydrodynamics. Further details of the numerical method can be found in an earlier study [37] and our previous publications [28,30]. The accuracy and fidelity of the numerical method have been validated using various canonical problems in these studies.

By applying the axisymmetric fluid-structure interaction model, we numerically examine the dynamics of the system described in Fig. 2. The concentration of our simulation is on the effect of the auxiliary inlet, whose opening and closing actions are controlled by the passive valve.

In our design, the valve opens during inflation so that the overall cross-sectional area of the flow inlet is considerably increased. The direct consequence is that the speed and kinetic energy of the ingoing flow during inflation are reduced. This helps lower the energy expenditure to refill the pressure chamber as well as the energy waste due to viscous dissipation. During deflation the valve is closed so that the outgoing flow leaves the body through the nozzle to create a jet flow for thrust production. Inspired by the morphology of a squid, this design is expected to decrease the energy expenditure and increase the propulsion efficiency of the system. On the other hand, the inclusion of the valve-controlled auxiliary inlet may also have some negative effects. First, it takes extra energy to achieve the opening and closing actions of the valve. Although the valve is passively activated through hydrodynamic load on it, its mechanical energy comes indirectly from the motion of the deforming body. Second, when deflation starts the valve will not be closed instantly due to its own inertia so that there will be fluid leaking from the auxiliary inlet. This will lessen the amount of momentum flux from the nozzle and reduce the thrust. An important purpose of this numerical study is to examine if the beneficial effect of the auxiliary inlet is able to outweigh its detrimental effect.

To normalize the problem, we choose three repeating variables: the contour length of the body L, the fluid density ρ, and the deformation period T. This is conveniently achieved by setting the values of these three parameters to be unity. In the following results the lengths are normalized by L, the speeds by LT^{-1}, the time by T, the masses by ρL^3, the forces by $\rho L^4 T^{-2}$, the power by $\rho L^5 T^{-3}$, and the vorticity by T^{-1}.

The normalized values of the physical parameters are listed in Table I. With this set of parameters, the area of the auxiliary inlet is about 2.8 times that of the exit of the nozzle. The values of the dimensionless parameters are the stroke ratio $\Gamma_m \equiv 4\Delta\forall/(\pi D^3) = 9.85$ ($\forall$ is the internal volume and $\Delta\forall$ is the total discharged volume during deflation) and the jet-related Reynolds number $R_{ej} \equiv \rho D\tilde{u}/\mu = 331$ [$\tilde{u}$ is the peak value of the spatially averaged outflow speed at the exit of the nozzle obtained as $(d\forall/dt)/(\pi D^2/4)|_{\max}$].

Based on numerical tests conducted in previous studies [28,38], the following numerical parameters are chosen: the size of the computational domain is 5×1; the lengths of the finest fluidic
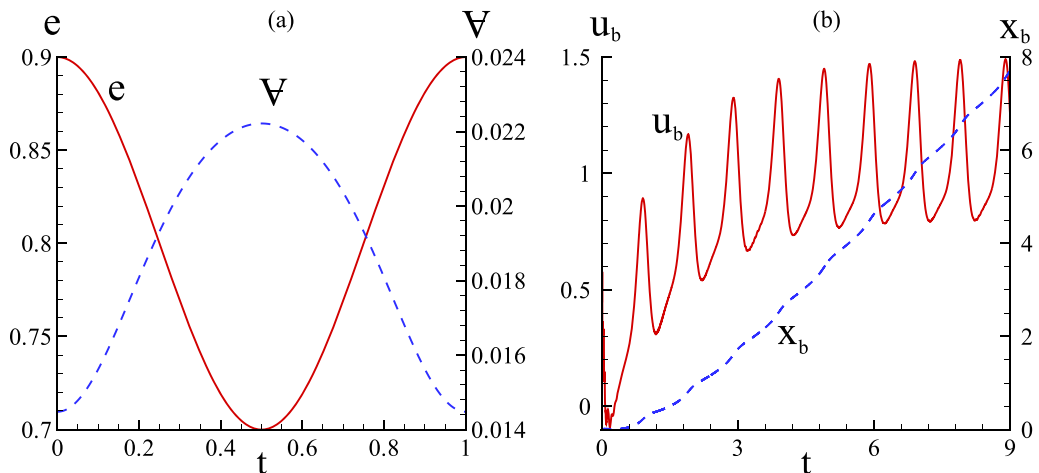
FIG. 3. (a) Variations of the eccentricity e and the internal volume $\forall$ of the shell during one deformation cycle. (b) Time histories of the forward speed u_b and the forward displacement x_b. The valve remains closed.

grid near the body in the longitudinal and radial directions are $\Delta x = \Delta r = 0.003$; the number of structural grids on the body (including the valve and the nozzle) is 350; the time step is $\Delta t = 10^{-4}$.

In practice, a uniform incoming flow with speed u_0 is introduced so that the swimming object does not leave the computational domain. The exact value of u_0 is obtained via tests. This is equivalent to the scenario in which the problem is considered in a reference system which moves in the swimming direction at a constant speed u_0. The effect of u_0 is removed during postprocessing so that the results we present are all measured in a fixed reference system without incoming flow.

IV. RESULTS

We first study a benchmark case in which the auxiliary inlet is kept closed so that $\theta \equiv 0$. It is then compared with a case with a mobile valve so that the effect of the auxiliary inlet can be illustrated. Finally, we examine effects of the design properties of the valve, i.e., the stiffness k_θ of the torsional spring and the rotational inertia I_θ of the valve itself.

A. Benchmark case ($\theta \equiv 0$)

We start by considering a case in which the valve is kept closed so that the exit of the nozzle serves both as the outlet during deflation and the inlet during inflation.

Figure 3(a) displays variations of the eccentricity e and the internal volume $\forall$ in one deformation cycle. It is clear that within the inflation phase ($0 \leqslant t < 0.5$) the eccentricity e decreases from $e_0 = 0.9$ to $e_1 = 0.7$. Meanwhile the internal volume $\forall$ increases monotonically so that fluid is sucked into the chamber. In the deflation phase ($0.5 \leqslant t \leqslant 1$) the eccentricity e decreases from e_1 to e_0. This causes the decline of the internal volume $\forall$. As a result fluid is expelled through the nozzle to generate thrust.

The cyclic shell deformation and the intermittent jet it creates lead to a forward motion u_b and a displacement x_b in the $-x$ direction, as demonstrated in Fig. 3(b). Based on the time history of u_b it is seen that steady-state cyclic response is reached after five to six deformation cycles. Hereafter the results we present are obtained during the ninth cycle of body deformation when the steady-state response has already been established in all the cases we study. For convenience when these results are presented the starting time is shifted to zero.

Next we consider the pathway of energy during an inflation-deflation cycle. As pointed out in [25], during inflation work done by the expanding shell is transformed into the kinetic energy of
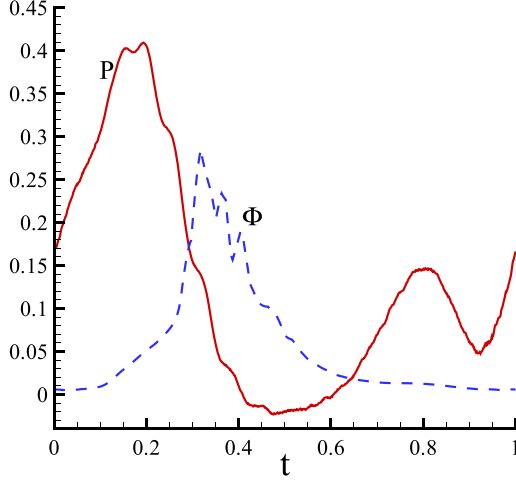
FIG. 4. Variations of the power expenditure P and the rate of viscous dissipation Φ during one deformation cycle. The valve remains closed.

the fluid outside of the body and that of the ingoing flow. Similarly, when deflation starts the shrinking shell powers the outgoing flow leaving the chamber. Since the ingoing flow is in the opposite direction of the jet, its kinetic energy is useless during the jetting phase. In fact, our previous simulations show that there is significant energy waste inside the body due to viscous dissipation. Hereby the rate of energy dissipation Φ inside the body is obtained as

$$\Phi = \int_{\Omega} \phi d\mathbf{x}, \tag{9}$$

where Ω is the internal volume within enclosed by the shell, the auxiliary inlet, and the nozzle. ϕ is given as

$$\phi = 2\mu \left[\left(\frac{\partial u_r}{\partial r} \right)^2 + \left(\frac{u_r}{r} \right)^2 + \left(\frac{\partial u_x}{\partial x} \right)^2 \right] + \mu \left(\frac{\partial u_x}{\partial r} + \frac{\partial u_r}{\partial x} \right)^2. \tag{10}$$

In Fig. 4 we plot variations of the power expenditure P and the rate of viscous dissipation Φ within one deformation cycle. In this particular case 48% of the mechanical energy transferred from the shell to the fluid during inflation is dissipated away inside the chamber due to viscosity within the same period ($0 \leqslant t < 0.5$; most of the dissipation occurs when $0.3 < t < 0.5$). On the other hand, during the deflation phase ($0.5 \leqslant t \leqslant 1$) the dissipation is much less significant in comparison with the energy expenditure.

The effect of dissipation can also be illustrated in the vorticity fields shown in Fig. 5. According to the left column in that figure, during inflation the ingoing flow generates strong vortices inside the chamber. By the end of the inflation phase at $t = 0.5$, these vortices are considerably weakened due to dissipation. Further dissipation of these internal vortices continues into the deflation phase. By the end of the cycle these is almost no viscosity inside the chamber.

The time-averaged forward speed $\bar{u}_b$ of this case is 1.03, and the cost of transport C_{trans} is 0.126. An animation showing the body motion or deformation and the flow field evolution in this case is included in the Supplemental Material [39].

B. Performance enhancement by using the auxiliary inlet

To study the effect of the auxiliary inlet on the dynamics of the system, we first focus on a case with $k_\theta = 10^{-6}$ and $I_\theta = 10^{-6}$. In Fig. 6(a), it is seen that this passive valve is successfully opened
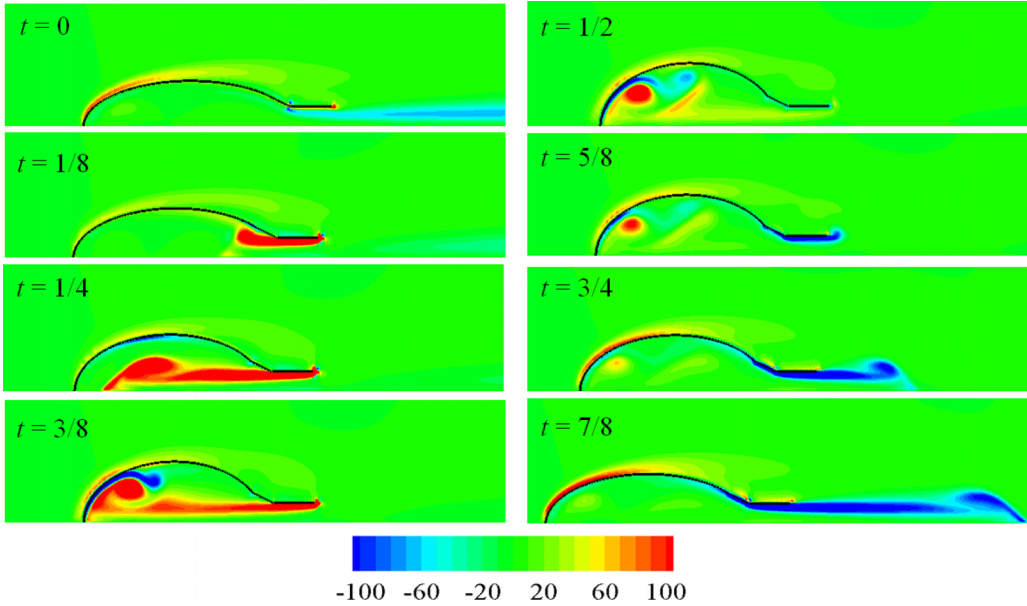
FIG. 5. Snapshots of the flow field around the body visualized through the vorticity contour over one cycle in steady state. Concentration of positive vorticity corresponds to the clockwise vortex, and negative vorticity corresponds to the counterclockwise vortex. The valve remains closed.

at the beginning of the inflation phase and closed at the beginning of the deflation phase by the hydrodynamic load on it.

The effect of the auxiliary inlet on the forward speed is shown in Fig. 6(b). For comparison the corresponding result from the benchmark case is also included. The most notable effect is that it reduces the deceleration at the beginning of the inflation phase as well as the acceleration during deflation. When t is around 0.7, the closing action of the valve creates some disturbance. The mean forward speed $\overline{u}_b$ of this case is 1.006, which is 2.3% lower in comparison with that of the benchmark case discussed in Sec. IV A.

During inflation, if there is not much delay in the opening action of the valve, only a small portion of mass flux goes through the nozzle since its cross-sectional area is much smaller than that of the auxiliary inlet. On the other hand, during deflation most of the outgoing flow moves through the nozzle. However, in this phase there could still be a certain amount of leaking from the auxiliary inlet since the valve cannot be closed instantly so that the thrust generation may be compromised. To depict this effect, we define a new parameter, the mass flow ratio during deflation m_{out}. This parameter represents the portion of outgoing mass flux through the nozzle, i.e., $m_{\mathrm{out}} = m_{\mathrm{nozzle}}/m_{\mathrm{total}}$, where m_{nozzle} is the mass of fluid leaving the system through the nozzle during deflation and m_{total} is the total mass of fluid discharged during deflation. In the benchmark case with fixed valve $m_{\mathrm{out}} = 1$. With the mobile valve, for better performance m_{out} should be as close to 1 as possible. In the current case the value of m_{out} is 0.86.

In comparison with its effect on u_b, the effect of the auxiliary inlet on the power expenditure P is much more pronounced. Specifically, during inflation there is a significant cutback in P, whereas during deflation despite the oscillations in the time history of P associated with the valve motion there is not much change in its magnitude. Quantitatively, in comparison with the benchmark case, when the auxiliary inlet functions the time-averaged value of P over one cycle is reduced from 0.13 to 5.07×10^{-2}, and C_{trans} decreases from 0.126 to 5.05×10^{-2}.

Since the auxiliary inlet diminishes the speed and kinetic energy of the ingoing flow, the rate of energy dissipation Φ in the chamber during inflation also drops dramatically, as demonstrated in
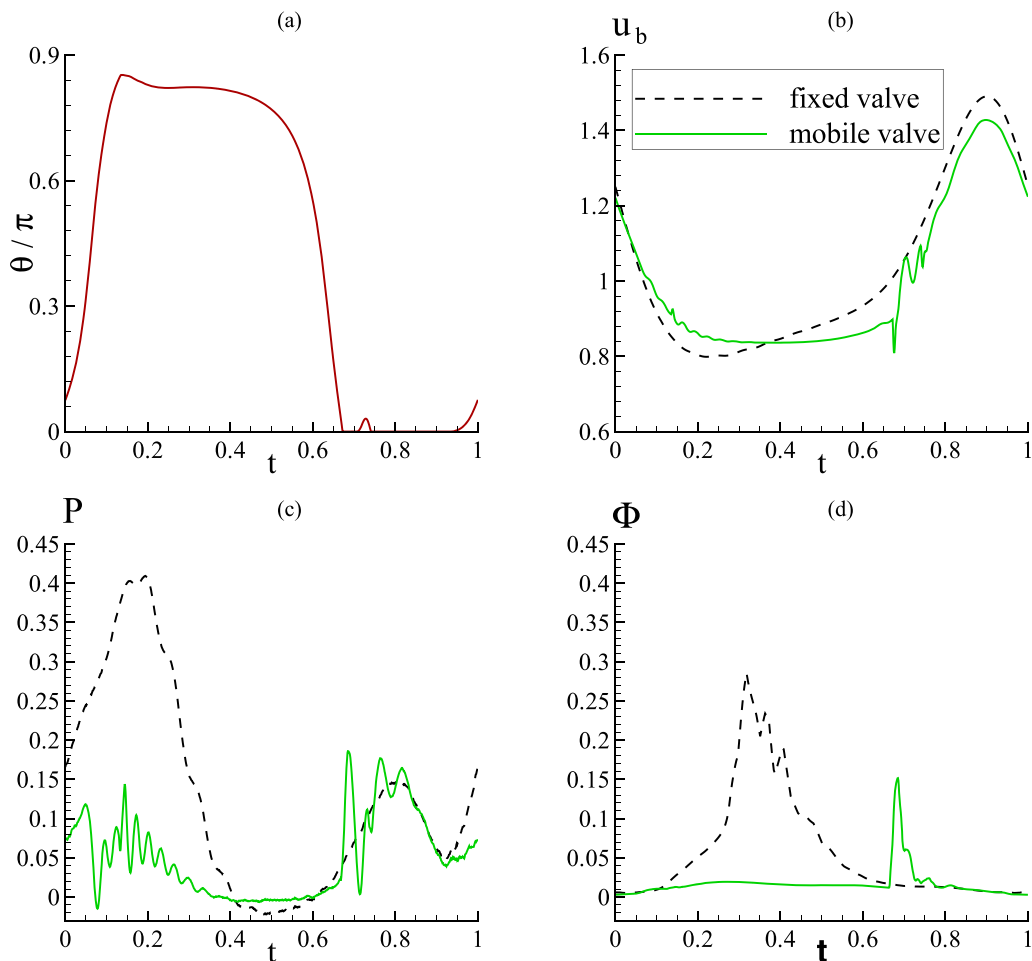
FIG. 6. Variations of (a) the rotational angle θ of the valve when it is mobile, (b) the forward speed u_b, (c) the power expenditure P, and (d) the rate of energy dissipation due to viscosity Φ during one cycle. The fixed-valve case is the benchmark case discussed in Sec. IV A. In the mobile-valve case $k_\theta = 10^{-6}$ and $I_\theta = 10^{-6}$.

Fig. 6(d). On the other hand, when deflation starts the closing action of the valve creates a spike in the time history of Φ near $t = 0.7$. However, since this spike only lasts for a relatively short time its contribution to the total energy loss is not large. Indeed, without the auxiliary inlet the total energy loss due to dissipation in the chamber over one cycle is around 5.6×10^{-2}. With the auxiliary inlet this value drops to 1.7×10^{-2}.

Figure 7 demonstrates snapshots of the flow field in and around the system with auxiliary inlet. By comparing this figure with Fig. 5, it is clear that the auxiliary inlet greatly diminishes the strength of the vortices inside the chamber during inflation (the two figures share the same contour range). This is consistent with the finding that in the inflation phase the rate of energy dissipation is mitigated.

In the Supplemental Material [39] there is another animation which demonstrates the body deformation (including the opening and closing actions of the valve) and the flow field in this case.
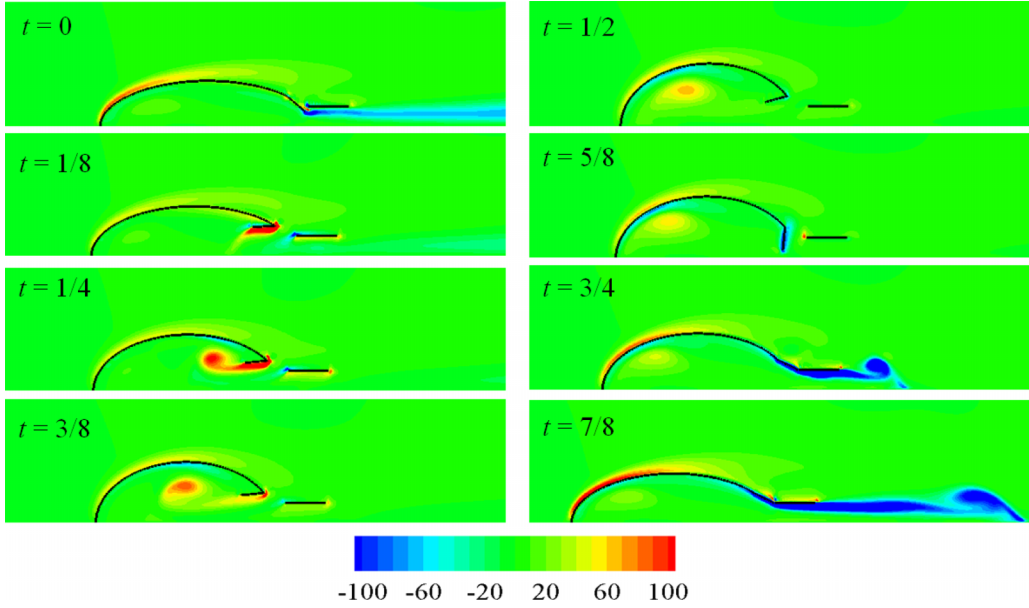
FIG. 7. Snapshots of the flow field around the body visualized through the vorticity contour over one cycle in steady state. The valve is rotatable with $k_\theta = 10^{-6}$ and $I_\theta = 10^{-6}$.

C. Effects of the properties of the valve

To explore the effects of the physical design of the valve, characterized by its rotational stiffness k_θ and rotational inertia I_θ, we conduct a parametric study to illustrate the impact of these two parameters upon the dynamics of the system.

Systematic simulations have been carried out within the parametric space of $10^{-7} \leqslant k_\theta \leqslant 10^{-3}$ and $10^{-6} \leqslant I_\theta \leqslant 10^{-4}$. The range of I_θ is relatively small since the dynamics of the system is more sensitive to this parameter. When I_θ is below this range, the simulation becomes unstable. If it is above this range, the deterioration in performance is too significant.

In Fig. 8(a) we plot dependencies of the mean forward speed $\overline{u}_b$ and the mass flow ratio m_{out} upon the rotational inertia I_θ of the valve when its rotational stiffness k_θ is fixed at 10^{-6}. It is seen that when I_θ rises from 10^{-6} to 10^{-4}, $\overline{u}_b$ drops dramatically from 1.01 to 0.48. This is mostly attributed to the decline in m_{out} at higher values of I_θ, i.e., with a heavier valve less fluid is discharged through the nozzle during jetting. In fact, when $I_\theta = 10^{-6}$, $m_{\text{out}} = 0.86$. However, when $I_\theta = 10^{-4}$, m_{out} is only 0.36 so that the jet flow created by each contraction becomes much weaker.

To explain the drop of m_{out} with heavier valves, in Fig. 8(b) we display time histories of the rotational angle θ at three different values of I_θ, 10^{-6}, 10^{-5}, and 10^{-4}. As I_θ is raised from 10^{-6} to 10^{-5}, it takes significantly more time for the valve to close, and correspondingly m_{out} decreases from 0.86 to 0.56. When $I_\theta = 10^{-4}$, the valve is not able to fully close at all so that m_{out} is further reduced to 0.36.

In addition to the decrease of m_{out} and the subsequent decrease in $\overline{u}_b$, heavier valves also consume more energy to activate as demonstrated in Fig. 9(a). In that figure we see that the mean power expenditure $\overline{P}$ increases with I_θ. For example, when $I_\theta = 10^{-6}$ the value of $\overline{P}$ is 0.051. It becomes 0.074 at $I_\theta = 10^{-5}$ and 0.091 at $I_\theta = 10^{-4}$.

The case when $I_\theta = 10^{-4}$ deserves more attention. Intuitively, as shown in Fig. 8(b), in this case the valve rotates within a smaller range of θ in comparison with the other two cases so that it might consume less energy to move it, which is true during the deflation phase [see Fig. 9(b) when
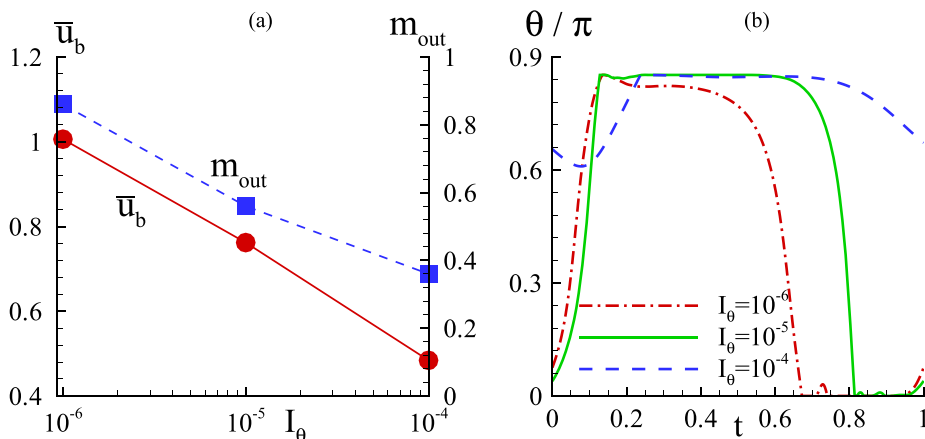
FIG. 8. (a) Dependencies of the mean forward speed $\bar{u}_b$ and the mass flow ratio m_{out} upon the rotational inertia I_θ of the valve. (b) Time histories of the rotational angle θ within one deformation cycle with different values of I_θ. $k_\theta = 10^{-6}$.

$0.5 < t < 1$]. However, in the same figure we see that during inflation the energy consumption in this case is higher than other cases so that its mean power expenditure is actually larger.

To explain this phenomenon, in Fig. 10 we show the snapshots of the near-body flow field in the heavy valve case (i.e., $I_\theta = 10^{-4}$). During inflation the heavy valve moves so slowly that it blocks the ingoing flow from both the nozzle and the auxiliary inlet. As a result it creates much stronger vortices during inflation (e.g., at $t = 3/8$ and $1/4$) in comparison with the case with a light valve (see Fig. 7; the two figures share the same contour range), which are eventually dissipated. Therefore, this heavy valve case involves more energy loss than the cases with lighter valves.

Figure 10 also shows that during deflation in this heavy valve case the jet out of the nozzle is weak in comparison with the one out of the auxiliary inlet (see the snapshots at $t = 3/4$ and $7/8$). It explains the slower swimming speed in this case. In fact, even though the mean power expenditure in this case (0.091) is still lower than the one in the benchmark case (0.13), there is a considerable
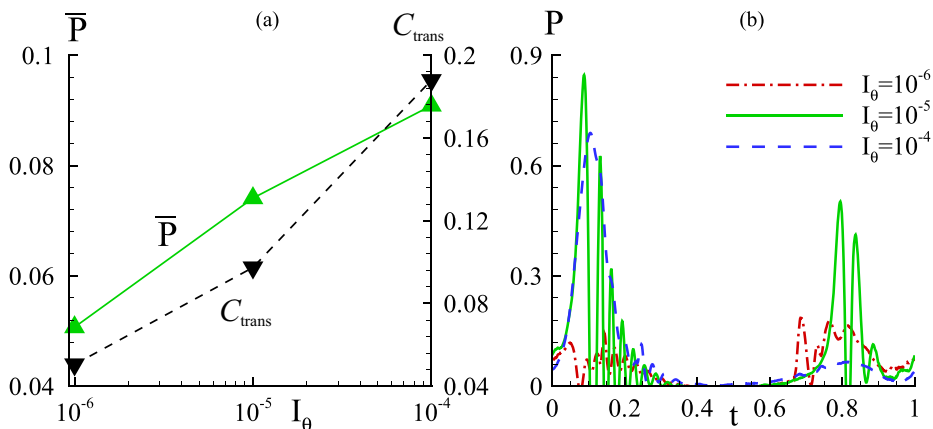
FIG. 9. (a) Dependencies of the mean power expenditure $\bar{P}$ and the cost of transport C_{trans} upon the rotational inertia I_θ of the valve. (b) Time histories of the instantaneous power expenditure P within one deformation cycle with different values of I_θ. $k_\theta = 10^{-6}$.
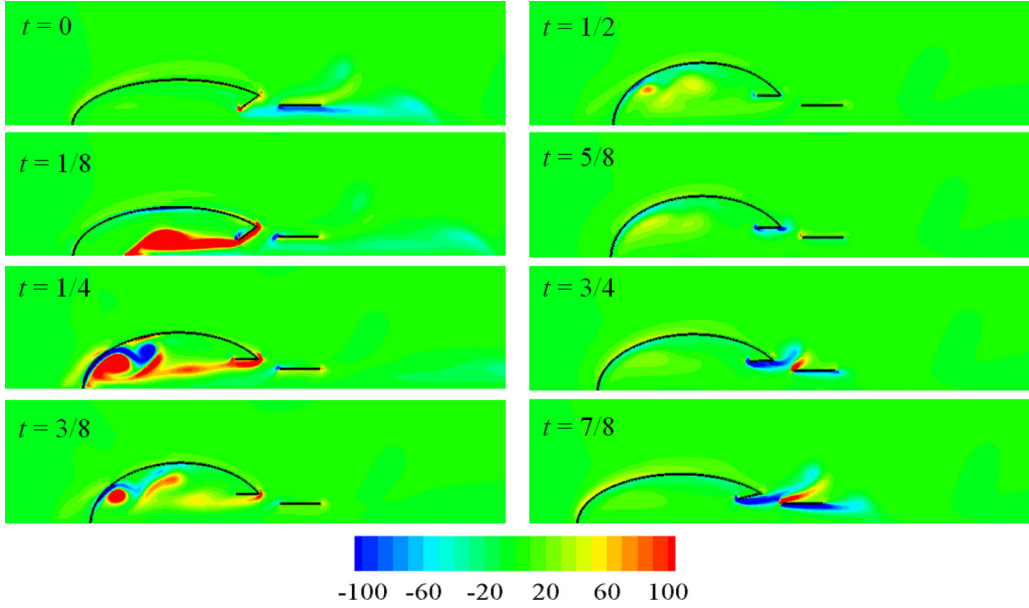
FIG. 10. Snapshots of the flow field around the body visualized through the vorticity contour over one cycle in steady state. The valve is rotatable with $k_\theta = 10^{-6}$ and $I_\theta = 10^{-4}$.

increase in its C_{trans} (0.188 versus 0.126 in the benchmark case) due to the decline in swimming speed.

The effect of k_θ is more complicated. According to our numerical results, when the value of k_θ is below 10^{-5}, its impact is insignificant. Above that, there are at least two contradicting effects. On the one hand, a stiffer spring brings down the energy expenditure during deflation and expedites the valve closing action when deflation starts, which boosts m_{out} and benefits thrust generation. On the other hand, such a spring increases the energy expenditure to open it and also slows down the opening action when inflation starts so that the ingoing flow might be blocked. Combining these effects, the impact of k_θ on C_{trans} is usually negative.
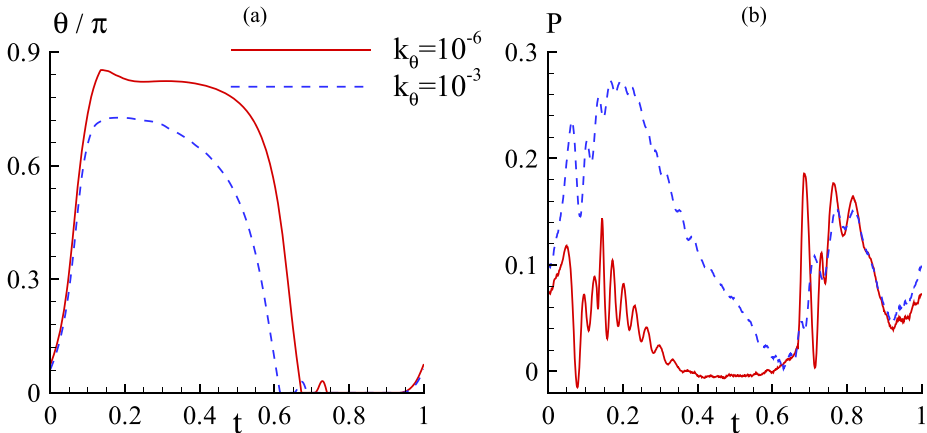
FIG. 11. Time histories of (a) the rotational angle θ of the valve and (b) the power expenditure within one deformation cycle with different values of k_θ. $I_\theta = 10^{-6}$.
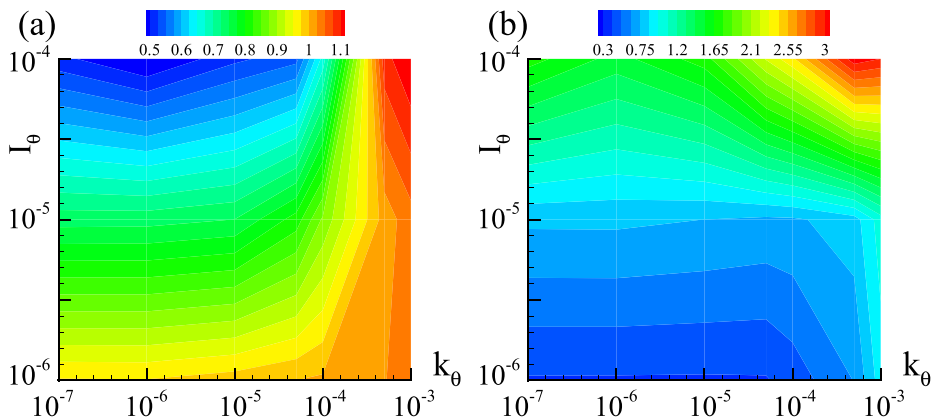
FIG. 12. Variations of (a) $\bar{u}_b/\bar{u}_{b0}$ and (b) $C_{\text{trans}}/C_{\text{trans0}}$ at different combinations of k_θ and I_θ. Here $\bar{u}_{b0} = 1.03$ and $C_{\text{trans}} = 0.126$ are the mean forward speed and C_{trans} of the benchmark case with fixed valve.

For example, in Fig. 11(a) we plot the time histories of the rotational angle θ of the valve with two different valves of k_θ (10^{-6} and 10^{-3}) when I_θ is fixed at 10^{-6}. It is seen that with a stiffer valve the auxiliary inlet does not open so wide during inflation. However, it closes faster during deflation so that the value of m_{out} increases from 0.86 at $k_\theta = 10^{-6}$ to 0.95 at $k_\theta = 10^{-3}$. Correspondingly, there is a 6.9% increase in mean forward speed $\bar{u}_b$. However, this gain in swimming speed is achieved at the cost of larger power expenditure P during inflation, as shown in Fig. 11(b). Specifically, the mean power expenditure $\bar{P}$ rises from 0.051 at $k_\theta = 10^{-6}$ to 0.125 at $k_\theta = 10^{-3}$. The net effect is a 127% increase in C_{trans}.

The locomotion performance of the system, characterized by its mean swimming speed $\bar{u}_b$ and C_{trans}, is displayed in Fig. 12. With I_θ fixed, when k_θ is below 10^{-5} the dependencies of $\bar{u}_b$ and $\bar{P}$ upon k_θ are relatively weak so that C_{trans} remains more or less unchanged as k_θ varies. Above that range, both $\bar{u}_b$ and $\bar{P}$ rise when k_θ is increased. As mentioned earlier, the increase in $\bar{u}_b$ at larger k_θ is outpaced by the dramatic increase in energy expenditure, leading to a fast increase of C_{trans}. When both I_θ and k_θ are large, there exist scenarios of relatively high values of $\bar{u}_b$, yet the efficiency is low. In these cases the valve has sufficient inertia to push the fluid even after the potential energy in the spring is mostly released. It works like a paddle to generate additional thrust during deflation. It is seen that in order for this system to outperform the benchmark case in terms of C_{trans}, both k_θ and I_θ should remain small (e.g., $k_\theta < 10^{-4}$, $I_\theta < 10^{-5}$). When I_θ remains as small as 10^{-6}, there is little loss in swimming speed as well.

V. CONCLUSION

In this paper we propose a performance enhancement mechanism for a bioinspired jetting system using an auxiliary flow inlet controlled by a one-way valve. The propulsion is achieved by periodic refilling and discharging of a pressure chamber inside the body accompanying its expansion and contraction deformations. The auxiliary inlet reduces the kinetic energy of the refilling flow and the subsequent energy dissipation in the pressure chamber. However, it takes extra energy to activate the valve that controls the opening and closing actions of the auxiliary inlet. It also reduces the mass and momentum flux through the nozzle during jetting.

By using an axisymmetric numerical model based on the immersed-boundary framework, we have investigated this problem computationally with an idealized model. Our results indicate that the performance of the auxiliary inlet relies heavily on the design of the valve, characterized by its rotational stiffness and inertia. If the valve is properly designed, the auxiliary inlet greatly diminishes the energy expenditure with minimum impact on the swimming speed so that the cost of transport

decreases. However, a poorly designed valve (e.g., a valve that is too heavy) could slow down the system so much that the cost of transport increases even if the energy expenditure is reduced. Stiffer valves benefit the swimming speed since they close more quickly to prevent leaking, but it takes more energy to activate these valves so that the net influence on the efficiency is not necessarily positive.

In the present paper the time history of the body deformation is prescribed, whereas in real systems it is often the power input that is given. In the latter scenario the introduction of the auxiliary inlet is expected to shorten the duration of the refilling process so that the swimming speed can be improved. Additional studies, including comprehensive modeling of the coupled fluid-structure-activation problem, are needed in this direction.

Finally, it is necessary to mention that the impact of the auxiliary inlet is also affected by other factors, such as the size, shape, and position of these openings. Besides, the design of the valve has been idealized in our current model, although the results are still qualitatively relevant since our valve includes two important characteristics, the inertia and the stiffness, that are shared by a wide range of valve designs. However, for the development of an actual system, a thorough parametric study based on its detailed design is necessary.

---

[1] F. Ahmed, M. Waqas, B. Jawed, A. Soomro, S. Kumar, A. Hina, U. Khan, K.K.Kim, and K. Choi, Decade of bio-inspired soft robots: A review, Smart Mater. Struct. **31**, 073002 (2022).

[2] S. Youssef, M. Soliman, M. Saieh, M. Mousa, M. Elsamanty, and A. Radwan, Underwater soft robotics: a review of bioinspiration in design, actuation, modeling, and control, Micromachines **13**, 110 (2022).

[3] B. Gemmell, J. Costello, S. Colin, C. Stewart, J. Dabiri, D. Tafti, and S. Priya, Passive energy recapture in jellyfish contributes to propulsive advantage over other metazoans, Proc. Natl. Acad. Sci. USA **110**, 17904 (2013).

[4] G. Weymouth, V. Subramaniam, and M. Triantafyllou, Ultra-fast escape maneuver of an octopus-inspired robot, Bioinspir. Biomim. **10**, 016016 (2015).

[5] F. Renda, F. Giorgio-Serchi, F. Boyer, and C. Laschi, Modelling cephalopod-inspired pulsed-jet locomotion for underwater soft robots, Bioinspir. Biomim. **10**, 055005 (2015).

[6] F. Giorgio-Serchi, A. Arienti, and C. Laschi, Underwater soft-bodied pulsed-jet thrusters: actuator modeling and performance profiling, Int. J. Robotics Res. **35**, 1308 (2016).

[7] X. Bi and Q. Zhu, Fluid-structure interaction of a squid-inspired swimmer, Phys. Fluids **31**, 101901 (2019).

[8] C. Christianson, Y. Cui, M. Ishida, X. Bi, Q. Zhu, G. Pawlak, and M. Tolley, Cephalopod-inspired robot capable of cyclic jet propulsion through shape change, Bioinspir. Biomim. **16**, 016014 (2020).

[9] N. Xu, Squid-inspired robots perform swimmingly, Sci. Robotics **6**, eabf4301 (2021).

[10] Q. Zhu and Q. Xiao, Physics and applications of squid-inspired jetting, Bioinspir. Biomim. **17**, 041001 (2022).

[11] J. Gosline and M. DeMont, Jet-propelled swimming in squid, Sci. Am. **252**, 96 (1985).

[12] H. Neumeister, B. Ripley, T. Preuss, and W. F. Gilly, Effects of temperature on escape jetting in the squid, J. Exp. Biol. **203**, 547 (2000).

[13] K. Muramatsu, J. Yamamoto, T. Abe, K. Sekiguchi, N. Hoshi, and Y. Sakurai, Oceanic squid do fly, Mar. Biol. **160**, 1171 (2013).

[14] R. O'Dor, J. Stewart, W. Gilly, J. Payne, T. Borges, and T. Thys, Squid rocket science: How squid launch into air, Deep Sea Research Part II: Topical Studies in Oceanography **95**, 113 (2013).

[15] C. Wardle, Limit of fish swimming speed, Nature (London) **255**, 725 (1975).

[16] R. Alexander, Swimming, in *Mechanics and Physiology of Animal Swimming*, edited by R. Alexander and G. Goldspink (Chapman and Hall, London, 1977), pp. 222–248.

[17] R. O'dor and D. Webber, Inverterate athletes: Trade-offs between transport efficiency and power density in cephalopod evolution, J. Exp. Biol. **160**, 93 (1991).

[18] F. Giorgio-Serchi, A. Lidtke, and G. Weymouth, A soft aquatic actuatir for unsteady peak power amplification, IEEE/ASME Trans. Mechatron. **23**, 2968 (2018).

[19] T. Wang, A. Lidtke, F. Giorgio-Serchi, and G. Weymouth, Manoeuvring of an aquatic soft robot using thrust-vectoring, in *2019 2nd IEEE International Conference on Soft Robotics (RoboSoft), Seoul, Korea* (IEEE, Piscataway, NJ, 2019), pp. 186-191.

[20] Y. Luo, Q. Xiao, Q. Zhu, and G. Pan, Thrust and torque production of a squid-inspired swimmer with a bent nozzle for thrust vectoring, Bioinspir. Biomim. **17**, 066011 (2022).

[21] T. Bujard, F. Giorgio-Serchi, and G. Weymouth, A resonant squid-inspired robot unlocks biological propulsive efficiency, Science Robotics **6**, eabd2971 (2021).

[22] Z. Yang, D. Chen, D. Levine, and C. Sung, Origami-inspired robot that swims via jet propulsion, IEEE Robotics and Automation Letters **6**, 7145 (2021).

[23] K. Schmidt-Nielsen, Locomotion: Energy cost of swimming, flying, and running, Science **177**, 222 (1972).

[24] F. Giorgio-Serchi, A. Lidtke, and C. Laschi, Biomimetic vortex propulsion: toward the new paradigm of soft unmanned underwater vehicles, IEEE/ASME Trans. Mechatron. **18**, 484 (2012).

[25] X. Bi and Q. Zhu, Role of internal flow in squid-inspired jet propulsion, Phys. Fluids **34**, 031906 (2022).

[26] X. Bi, H. Tang, and Q. Zhu, Valve-mediated flow control in salp-like locomotion, Phys. Fluids **34**, 051913 (2022).

[27] X. Bi, H. Tang, and Q. Zhu, Feasibility of hydrodynamically activated valves for salp-like propulsion. Phys. Fluids **34**, 101903 (2022).

[28] X. Bi and Q. Zhu, Pulsed-jet propulsion via shape deformation of an axisymmetric swimmer, Phys. Fluids **32**, 081902 (2020).

[29] X. Bi and Q. Zhu, Free swimming of a squid-inspired axisymmetric system through jet propulsion, Bioinspir. Biomim. **16**, 066023 (2021).

[30] X. Bi and Q. Zhu, Effect of nozzle geometry on the performance of pulsed-jet propulsion at low Reynolds number, J. Fluids Struct. **107**, 103402 (2021).

[31] C. Peskin, The immersed boundary method, Acta Numerica **11**, 479 (2002).

[32] B. Griffith and N. Patankar, Immersed methods for fluid–structure interaction, Annu. Rev. Fluid Mech. **52**, 421 (2020).

[33] W. Huang, S. Shin, and H. Sung, Simulation of flexible filaments in a uniform flow by the immersed boundary method, J. Comput. Phys. **226**, 2206 (2007).

[34] W. Huang and H. Sung, An immersed boundary method for fluid-flexible structure interaction, Comput. Methods Appl. Mech. Eng. **198**, 2650 (2009).

[35] D. Goldstein, R. Handler, and L. Sirovich, Modelling a no-slip flow boundary with an external force field, J. Comput. Phys. **105**, 354 (1993).

[36] K. Shoele and Q. Zhu, Leading edge strengthening and the propulsion performance of flexible ray fins, J. Fluid Mech. **693**, 402 (2012).

[37] K. Kim, S. Baek, and H. Sung, An implicit velocity decoupling procedure for the incompressible Navier-Stokes equations, Int. J. Numer. Meth. Fluids **38**, 125 (2002).

[38] X. Bi and Q. Zhu, Efficiency of pulsed-jet propulsion via thrust-drag decomposition, Phys. Fluids **33**, 071902 (2021).

[39] See Supplemental Material at http://link.aps.org/supplemental/10.1103/PhysRevFluids.8.043101 for body motion, deformation, and flow field with or without the auxiliary inlet.